JOURNAL OF GEOPHYSICAL RESEARCH, VOL. ?, NO. ?, PAGES ?–?, MONTH ?, 2000

A method for assessing the quality of model-based estimates of ground temperature and atmospheric moisture using satellite data

Man Li C. Wu and Siegfried Schubert
Data Assimilation Office, Goddard Laboratory for Atmospheres, NASA GSFC, Greenbelt, Maryland

Ching I. Lin and Ivanka Štajner
General Sciences Corporation, NASA Goddard Space Flight Center, Greenbelt, Maryland

Abstract. A method is developed for validating model-based estimates of atmospheric moisture and ground temperature using satellite data. The approach relates errors in estimates of clear-sky longwave fluxes at the top of the Earth-atmosphere system to errors in geophysical parameters. The fluxes include clear-sky outgoing longwave radiation (CLR) and radiative flux in the window region between 8 and 12 μm (RadWn). The approach capitalizes on the availability of satellite estimates of CLR and RadWn and other auxiliary satellite data, and multiple global four-dimensional data assimilation (4-DDA) products. The basic methodology employs off-line forward radiative transfer calculations to generate synthetic clear-sky longwave fluxes from two different 4-DDA data sets. Simple linear regression is used to relate the clear-sky longwave flux discrepancies to discrepancies in ground temperature (δT_g) and broad-layer integrated atmospheric precipitable water (δpw). The slopes of the regression lines define sensitivity parameters which can be exploited to help interpret mismatches between satellite observations and model-based estimates of clear-sky longwave fluxes. For illustration we analyze the discrepancies in the clear-sky longwave fluxes between an early implementation of the Goddard Earth Observing System Data Assimilation System (GEOS2) and a recent operational version of the European Centre for Medium-Range Weather Forecasts data assimilation system. The analysis of the synthetic clear-sky flux data shows that simple linear regression employing δT_g and broad layer δpw provides a good approximation to the full radiative transfer calculations, typically explaining more than 90% of the 6 hourly variance in the flux differences. These simple regression relations can be inverted to "retrieve" the errors in the geophysical parameters. Uncertainties (normalized by standard deviation) in the monthly mean retrieved parameters range from 7% for δT_g to ~20% for the lower tropospheric moisture between 500 hPa and surface. The regression relationships developed from the synthetic flux data, together with CLR and RadWn observed with the Clouds and Earth Radiant Energy System instrument, are used to assess the quality of the GEOS2 T_g and pw. Results showed that the GEOS2 T_g is too cold over land, and pw in upper layers is too high over the tropical oceans and too low in the lower atmosphere.

1. Introduction

While much progress has been made to improve the climate characteristics of general circulation models (GCMs), the hydrological cycle stands out as a major component of the Earth-Atmosphere system which is still poorly modeled [e.g., *Gates et al.* 1999; *Lau et al.*, 1995]. Major advances in modeling the hydrological cycle are hampered by inadequate and/or incomplete measurements of such quantities as precipitation, latent heating, clouds, atmospheric and soil moisture, and ground temperature. Data obtained by methods of four-dimensional data assimilation (4-DDA) suffer from errors in these quantities, both as a result of errors in the assimilating models and a lack of observations to directly constrain the hydrological cycle.

Paper number 2000JD900478.

In this study we focus on methods to verify model-based (including 4-DDA) moisture profiles (q) and ground temperature (T_g) using satellite data. We focus on these two parameters because they are highly dependent on the parameterizations of sub-grid-scale processes, and they are difficult to validate because there are few reliable observations of these quantities with global coverage. The quality of the ground temperature directly reflects on the quality of the land surface formulation, while the moisture profiles are important constraints on the behavior of the boundary layer and convection schemes. The methodology described here was developed as the result of efforts to validate these quantities in a global data assimilation system, but the methodology should also prove useful for assessing systematic errors of global atmospheric models.

The basic methodology is as follows: First, sensitivity parameters are obtained by applying off-line forward radiative trans-

fer calculations to two different assimilated data products to relate differences in clear-sky longwave fluxes at the top of the Earth-atmosphere system to errors in geophysical parameters. The clear-sky longwave fluxes include clear-sky outgoing longwave radiation (CLR) and radiative flux in the window region between 8 and 12 μm (RadWn). The assimilated data sets should provide physically reasonable and global estimates of the geophysical fields. Any discrepancies in the fields from the two different systems measure our uncertainty and provide a tool for assessing the sensitivity of the CLR to discrepancies in these fields. The sensitivity parameters together with satellite estimates of clear-sky longwave fluxes (and other auxiliary satellite data) are then used to relate the clear-sky longwave fluxes to errors in the geophysical fields. For purpose of illustration, sensitivity parameters are obtained by comparing ground temperature and atmospheric temperature and moisture profiles from an early implementation of version 2 of the Goddard Earth Observing System (GEOS2) data assimilation system [*Data Assimilation Office* (DAO), 1996] with those quantities from a recent operational version of the European Centre for Medium-Range Weather Forecasts (ECMWF) data assimilation system [*Courtier et al.*, 1998].

The key satellite data used for this study are the CLR and RadWn estimates from the Clouds and Earth Radiant Energy System (CERES) [*Wielicki et al.*, 1996] instrument onboard the Tropical Rainfall Measurement Mission (TRMM).

This approach to validation is viewed as a compromise between a simple comparison of model-generated and observed CLR and RadWn and full retrieval algorithms that attempt to exploit information in multiple spectral bands to obtain estimates of the geophysical quantities. The method provides insight into the nature of the errors in the model-based CLR and RadWn consistent with the broadband nature of the CLR and RadWn satellite measurements.

Sections 2 describes the satellite data and radiative transfer model used for the forward calculation. The methodology is described in section 3. The sensitivity analysis, based on the GEOS2 and ECMWF assimilated data, is described in section 4. A comparison with the CERES/TRMM clear CLR and RadWn is presented in section 5. Discussion and conclusions are given in section 6.

2. Satellite Data and Radiative Transfer Model

The primary quantity analyzed in this study is the CLR and RadWn. The availability of high-quality satellite estimates of CLR and RadWn (see below) has made these important quantities for validating global models. Relating and understanding differences between model-computed and observed CLR and RadWn is complicated by a number of factors. Some of the differences arise from sampling differences and fundamental differences between satellite measurements and model "grid-scale" fields. In this study we focus on the problem of relating the errors (computed minus observed) in CLR and RadWn to deficiencies in the model-based estimates of the radiatively important geophysical quantities (e.g., atmospheric moisture and temperature and ground temperature). The methodology is developed with synthetic flux data to circumvent the sampling and representativeness problems. These issues are beyond the scope of this initial study, though they will need to be addressed when developing quantitative estimates of errors in the geophysical quantities based on satellite measurements. We note that in this study the model-based CLR and RadWn are computed in an off-line mode (see below). Many institutions now routinely compute CLR on-line during the course of model integrations.

In the following we describe the CLR and RadWn data, various other auxiliary data sets used for this study, and the radiative transfer scheme used for the off-line calculation of CLR and RadWn.

2.1. CLR and RadWn Satellite Data

While the sensitivity parameters will be developed with synthetic flux data (see next section), our application of the methodology to validating GEOS2 (see section 5) will require satellite observations as input. For the latter we have obtained CERES/TRMM data [*Wielicki et al.*, 1996]. The quality of the CERES data is comparable to the quality of the Earth Radiation Budget Experiment (ERBE) data for instantaneous radiance, fluxes, and scene type. Generally, radiance uncertainties are at the 1% level or less. Some differences between CERES/TRMM and ERBE-ERBS are as follows: the field of view resolution, the spectral response of the instruments, and the tropical only coverage of TRMM [*Wielicki et al.*, 1996].

2.2. Radiative Transfer Scheme

For the sensitivity calculations we employ the radiative transfer scheme developed by *Chou and Suarez* [1994]. This scheme is used in the GEOS2 model. The longwave (LW) calculation has nine bands (band 10 is added to compute flux reduction due to N_2O in the 15 μm region). The transmission and absorption of H_2O, H_2O continuum, CO_2, O_3, CFC, CH_4, and N_2O is modeled using k distribution. In the LW, multiplication approximation for bands are assumed. The LW scheme compares well with detailed line-by-line calculations. The root mean square (rms) errors of CLR are between 1 and 3 Wm^{-2} [*Chou and Kouvaris*, 1991; *Chou et al.*, 1995; *Kratz et al.*, 1998]. In addition, the code has been participated in the Intercomparison of Radiation Codes in Climate Models (ICRCCM) [*Ellingson et al.*, 1991].

Surface emissivity depends on surface property or vegetated surface. For a given surface type, its values are also different for different wavelengths in the LW spectrum. The global distribution of surface type and the associated emissivity that we used were taken from CERES. The Advanced Spaceborne Thermal Emission and Reflection Radiometer created an easily accessible data set on the basis of extensive measurements of the spectral reflectances of surface material in the 2–16 μm region by *Salisbury and D'Aria* [1992]. *Wilber et al.* [1999] derived spectrum emissivity from the spectrum reflectance on the basis of scene type. The scene type was determined by using a 1 km map of the International Geosphere Biosphere Program scene types as supplied by the U.S. Geological Survey (USGS). A scene type of tundra was added to separate it from desert resulting in 18 surface types. We calculate the fraction of each scene type in a 2° × 2.5° longitude and latitude box from the 1/6° equal angle data. Radiative fluxes are computed in each of the 2° × 2.5° boxes several times on the basis of the number of scene types in a box (maximum is 18). The final mean radiative flux is an area mean of the fractional type. Surface emissivity effect on CLR is large over the desert regions, where off-line computations show it can be as high as 5–8 Wm^{-2} (mostly from window bands).

2.3. Ozone

The analyzed ozone fields from the Goddard Earth Observing System (GEOS) ozone data assimilation system (DAS)

[*Riishøjgaard et al.*, 1999; *Štajner et al.*, 1999] are used in this study. They are obtained by assimilating total column ozone observations from the Total Ozone Mapping Spectrometer (TOMS) and ozone profile observations from the solar backscattered ultraviolet/2 (SBUV/2) instruments into an off-line transport model driven by the GEOS-DAS assimilated winds. While the statistical analysis of ozone is performed at every model time step (15 min) using a global physical space-based analysis scheme, the analyzed ozone is written out at the same frequency and resolution as the other GEOS-DAS fields. The high quality of the ozone fields is illustrated by two examples from their validation for January 1998. The average rms difference between TOMS observations and total column ozone forecast is about 11 Dobson units or 3.7% of the average total column ozone. The comparison of analyzed ozone profiles with independent ozone observations measured by the Halogen Occultation Experiment (HALOE) onboard the NASA Upper Atmosphere Research Satellite shows that the mean profiles agree within 3.2% between the pressures of 30 and 1 hPa. In this region the HALOE measurements agree within 5% with ozonesonde, lidar, balloon, rocketsonde, and other satellites ozone measurements [*Bruhl et al.*, 1996].

While the ozone contribution to CLR is relatively small, the accuracy of its distribution is critical for the CLR computation. In particular, the high ozone concentrations in the stratosphere and its presence in the water vapor window region are important for the clear-sky flux.

3. Methodology

To help understand the methodology, we start with the radiative transfer equations for clear-sky conditions in the LW region of the spectrum given

$$\mathrm{CLR}(T, q, T_g, \ldots) = \int_{\nu_1}^{\nu_2} \pi \varepsilon B_\nu(T_g)\tau_\nu(u_T)\, d\nu + \int_{\nu_1}^{\nu_2} (1-\varepsilon_\nu)\tau_\nu(u_T) \int_{u_T}^{u} \pi B_\nu(T(u')) \frac{d\tau_\nu(u'-u)}{du'}\, du'\, d\nu + \int_{\nu_1}^{\nu_2}\int_{0}^{u} \pi B_\nu(T(u')) \frac{d\tau_\nu(u-u')}{du'}\, du'\, d\nu, \quad (1)$$

where ν is frequency, B_ν is the Planck parameter, ε_ν is surface emissivity, τ_ν is the transmission parameter at frequency ν, u is the path length, and u_T is the total path length. In (1) the first terms on the right-hand side (RHS) is the contributions from the surface. The second term is the downwelling atmospheric radiation reflected from the surface. This term tends to be small compared to the other terms. The third term is the contribution from the atmosphere.

The first step is to develop sensitivity parameters relating CLR differences to differences in the geophysical quantities. This is carried out here using data from two different four-dimensional data assimilation systems. The simulated radiances are computed using the T_g, and q and temperature (T) profiles as input to the radiative transfer calculations using the scheme described in the previous section. The aim of this step is to try to understand which aspect of the input data is most sensitive to the CLR and how the sensitivity varies over the globe.

We consider a change in the CLR in terms of the following linearization:

$$\delta\mathrm{CLR}(T, q, T_g) \approx \frac{\partial \mathrm{CLR}}{\partial T_g}\delta T_g + \sum_i \frac{\partial \mathrm{CLR}}{\partial q_i}\delta q_i + \sum_i \frac{\partial \mathrm{CLR}}{\partial T_i}\delta T_i, \quad (2)$$

where δq_i and δT_i are the differences in the two moisture and temperature products in layer i. We consider the partial derivatives in (2) as sensitivity parameters relating changes in the geophysical quantities to changes in the CLR. The validity of this approximation will be examined in the following section by comparing results from the full radiative transfer calculations (referred to as the "true" values in the following discussions) with results from "best fit" linear regression equations based on (2).

4. Sensitivity Analysis

In this section we shall compute the sensitivity parameters defined previously using output from two different 4-DDA systems (GEOS2 and ECMWF). Note that since we are only interested in differences, there is no need in these calculations to assume one or the other 4-DDA systems is correct. In section 5 we will use the sensitivity parameters together with satellite data to validate the GEOS2 system.

GEOS2 represents a major upgrade to the baseline GEOS1 system employed in the NASA first reanalysis effort [*Schubert et al.*, 1993]. The final version of GEOS2 includes a physical-space three-dimensional variational analysis algorithm (Physical-Space Statistical Analysis System (PSAS) [*Cohn et al.*, 1998]) and numerous improvements to the general circulation model. The model improvements include a more accurate dynamics [*Takacs and Suarez*, 1996], a gravity wave drag scheme [*Zhou et al.*, 1996], improved diagnostic clouds, the mosaic land surface scheme of *Koster and Suarez* [1994], a level 2.5 moist turbulence scheme [*Helfand et al.*, 1999], and new SW and LW radiation code [*Chou and Suarez*, 1994]. The system also includes the capability to assimilate TOVS moisture and Special Sensing Microwave/Imager (SSM/I) total precipitable water.

The version of GEOS2 used here was run with 70 vertical layers extending to 0.01 hPa and with a spatial resolution of 2° × 2.5° latitude-longitude. The T_g output was saved every 3 hours, while the upper air T and q were saved every 6 hours. The GEOS2 data are compared with operational analyses generated by the ECMWF for January 1998. These data are available every 6 hours and have been interpolated to a 2° × 2.5° grid to be consistent with the GEOS2 data.

As described in the previous section, T_g, T, and q from both analyses are input to a radiative transfer model to compute the CLR and RadWn. The primary interest for this study is in the sensitivity to T_g and q. Our initial analysis showed that T differences between GEOS2 and ECMWF are small, and the effect on the computation of CLR is around ± 1.5 Wm^{-2}.

In the following, CLR computed by using all GEOS2 data is referred to as CLRGEOS2, and the CLR computed using all ECMWF data is referred to as CLRECMWF. Sensitivities are estimated by recomputing the CLR after replacing selected input fields. For example, to estimate $\partial\mathrm{CLR}/\partial T_g$, we compute the CLRGEOS2 as before but replacing the GEOS2 T_g with

the T_g from the ECMWF data. We will refer to this as CLRGEOS2(δT_g), indicating the calculation is carried out with the GEOS2 ground temperature perturbed by the amount $\delta T_g = T_g(\text{ECMWF}) - T_g(\text{GEOS2})$. The difference $\delta\text{CLR}(\delta T_g) = \text{CLRGEOS2}(\delta T_g) - \text{CLRGEOS2}$ which divided by δT_g is a measure of the sensitivity of CLR to ground temperature. For example, the change in CLR due to differences in T_g is then denoted by $\delta\text{CLR}(\delta T_g)$. An estimate of the sensitivity of CLR to T_g changes is

$$\frac{\partial \text{CLR}}{\partial T_g} \approx \frac{\delta\text{CLR}(\delta T_g)}{\delta T_g}. \quad (3)$$

Since the sensitivity of CLR to moisture varies with height, sensitivity ratios are estimated separately for different layers in the atmosphere. For these calculations we used ECMWF data as the basis for determining the moisture sensitivity since we felt that the ECMWF moisture values were more reasonable especially at upper levels. In principle, it should not matter which one is used (GEOS2 or ECMWF), since we are only after the sensitivity. In fact, tests showed similar results using GEOS2, though we felt the analysis using ECMWF provided results that were somewhat easier to interpret for the moisture. The layer-integrated moisture is referred to as the precipitable water (pw). For example, we compute $\delta\text{CLR}(\delta pw_h) = \text{CLRECMWF}(\delta pw_h) - \text{CLRECMWF}$. Here δpw_h is equal to pw from ECMWF minus pw from GEOS2, where pw_h is the moisture in the layer between 200 and 500 hPa. Similar calculations are done for moisture between 200 and 700 hPa (pw_{700}), between 200 and 900 hPa (pw_{900}), between 200 hPa and surface ($pw_{s/c}$), between 500 and surface (pw_l), and the full moisture profile (tpw). The sensitivities to pw are given by equations analogous to (3). For example,

$$\frac{\partial \text{CLR}}{\partial pw_h} \approx \frac{\delta\text{CLR}(\delta pw_h)}{\delta pw_h} \quad (4)$$

estimates the sensitivity of CLR to the pw between 200 and 500 hPa.

We use the period January 1998 to compute the sensitivity parameters, since we have in-house operational analyses from ECMWF for this time period. Unless noted otherwise, all calculations are based on 6 hourly data on the GEOS2 2° × 2.5° grid. We estimate the sensitivities locally using simple regression to relate the 6 hourly differences in CLR (or δCLR) to differences (δx) in the input quantities. For a single predictor the regression equation takes the form

$$\delta\text{CLR}(\delta x) = \alpha_x \delta x + \varepsilon, \quad (5)$$

where x is the quantity being varied (for example, T_g, pw_h, or pw_l), α_x is the sensitivity parameter to be estimated, and ε is the component of the δCLR not explained by δx.

Before computing the sensitivity parameters, we first examine the differences in the CLR from the two assimilated data sets and look in some detail at the various band contributions to the total CLR. Figure 1 shows the mean δCLR = CLRGEOS2 − CLRECMWF for January 1998 computed from the 6 hourly data. Over land the differences can be as large as 15–20 Wm^{-2} and over the oceans as large as 20–25 Wm^{-2}. Figures 1b and 1c show $\delta\text{CLR}(\delta T_g)$ and $\delta\text{CLR}(\delta q)$, respectively. The pattern and magnitude of the δCLR distribution over land is very close to $\delta\text{CLR}(\delta T_g)$, while over oceans, δCLR is very similar to $\delta\text{CLR}(\delta q)$. This indicates that for these two assimilated data sets the largest discrepancies in CLR over the land poleward of about 40° latitude are due to ground temperature differences, while the largest discrepancies in CLR over the oceans are due to differences in the moisture profiles.

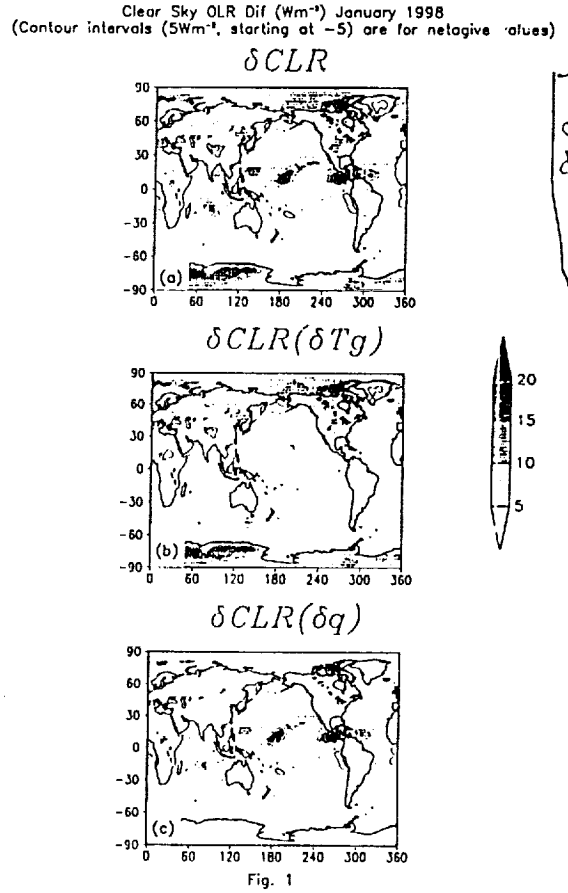

Fig. 1

Figure 1. Monthly mean δCLR (Wm^{-2}) based on the GEOS2 data and the ECMWF data: (a) differences induced by δT_g, δq, and δT; (b) differences induced by δT_g; and (c) differences induced by δq. Contours are for negative values; the intervals are the same as the shaded values.

To better understand the sources of the CLR from the atmosphere and land, we look in more detail at the various band contributions to the CLR (Figures 2 and 3). The gaseous absorption included in the radiative transfer code [*Chou and Suarez*, 1994] are H_2O, CO_2, O_3, and trace gases (see section 2.2). In the following we will focus on the water vapor effect. Column 1 in Figure 2 shows the CLR computed from the ECMWF data in each of the nine bands. The first three bands are the contributions from the water vapor rotational bands. The next three are the contributions from the 800 to 1215 cm^{-1} window region, and the last three represent contributions from water vapor vibration and rotation bands. Column 2 shows the emission from the surface ($\varepsilon_s T_g$). Column 3 is the contribution to the CLR from the first two terms on the RHS

Au: Please check reproduction quality of figures and make sure they are numbered correctly

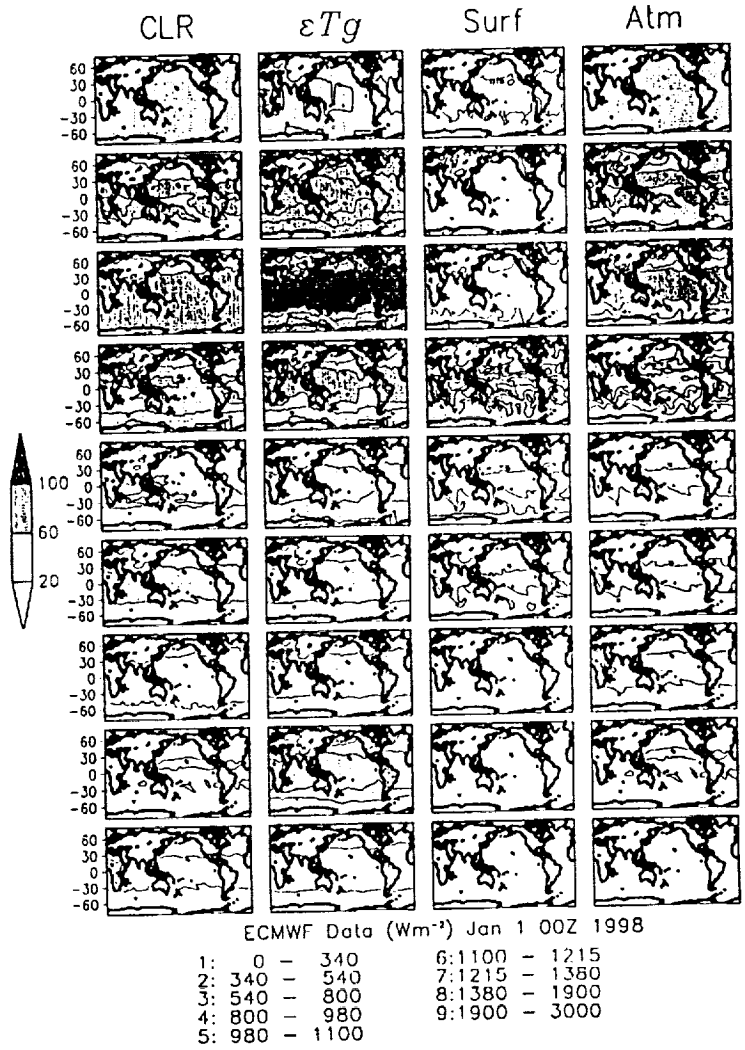

Figure 2. Contributions to CLR (Wm^{-2}) from different parts of the atmosphere and different bands. From top down the band ranges from band 1 to band 9, the wave number for each band is shown at the bottom of the figure. Value εT is surface emission, Surf (surface contribution) is the first two terms of the RHS of (1) and Atm (contribution from the atmosphere) is the third term of the RHS of (1). Contour intervals are 10 Wm^{-2} except the last one in a column, which is 5 Wm^{-2}.

of (1), and column 4 shows the contribution to the CLR from the atmosphere (third term on the RHS of (1)).

The strength of surface emission follows the Planck function which peaks in the third band (540–800 cm^{-1}). The intensity from the other bands decreases gradually toward both sides. Note that the band widths are not uniform. The atmospheric transmission function strongly modifies the surface emission, especially in bands with strong gaseous absorption. The degree of the atmospheric effect depends on the opacity of the atmosphere. Comparing, in Figure 2, the surface emission with the amount reaching the top of the atmosphere, we find a significant greenhouse effect due to gaseous absorption. The greenhouse effect is very strong in the water vapor rotational band ranging from zero to 800 cm^{-1} (which include the 15 μm CO_2 band) and the vibrational and rotational band ranging from 1215 to 3000 cm^{-1}. The largest contributions to CLR are from bands 2 to 4, ranging from 340 to 980 cm^{-1}, and most of the contributions are from the atmosphere because of the opacity of the water vapor rotational bands and CO_2 bands. For example, the surface has the largest emission in band 3, but the surface contribution to CLR is relatively small due to the opacity of the atmosphere. In particular, over the tropical oceans the surface contribution to the CLR from this band is about 5%, while the rest is from the atmosphere (see Figure 3). Figure 3 includes the effective pressure level of the contributions from the atmosphere averaged over the month. This is determined by finding the peak of the weighting function computed from the mean transmission functions. In bands 2 and 3, most contributions over land are from layers close to surface (lowest 300 hPa), while most contributions over the tropical

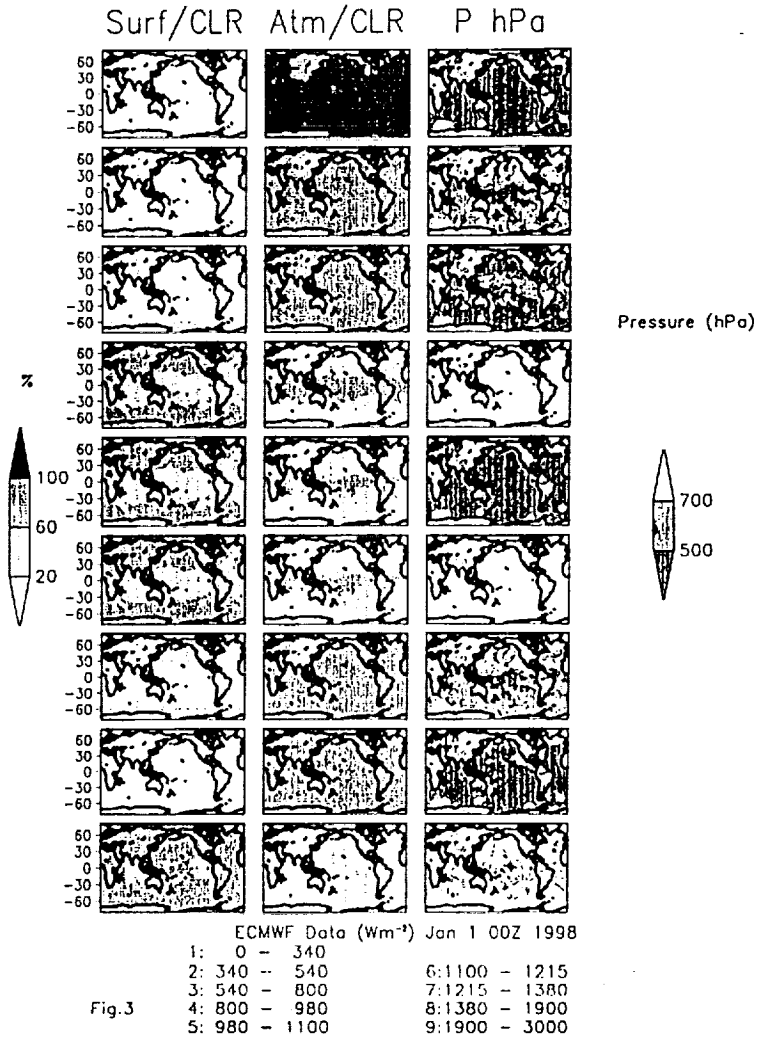

Figure 3. Percentage contributions to CLR (%) from Surf and Atm and mean peak of the weighting function (hPa).

oceans are from layers ranging from 200 to 500 hPa, where water vapor concentration is high. Away from the tropics the opacity decreases, and the layer of largest emission is lowered to between 500 and 700 hPa. In the tropics the atmosphere contributes more than the surface in all bands. The largest contributions are from between 200 to 500 hPa and some are from 500 to 700 hPa depending on the opacity of the atmosphere.

In summary, the major contribution to CLR over the tropical oceans (30°S to 10°N) is from the atmosphere between 200 and 500 hPa. In the subtropics the contribution tends to be from lower in the atmosphere between 500 and 700 hPa. Over land, for the Northern Hemisphere winter, most of the contribution to CLR is from the surface (from window bands) and from the lowest (300 hPa) layer of the atmosphere.

F4 Figure 4 shows the regression results for T_g (land only) for January 1998 based on 6 hourly data. We note that sea surface temperature (SST) is specified from observations in both analyses, and we do not consider any differences in the SST data. The regression is carried out on the CLR differences resulting from perturbing only the ground temperature using the radiative transfer equation (1). The extent to which the regression explains the results from the full radiative transfer calculation is thus a measure of the adequacy of the linear approximation for the effect of T_g. The estimated sensitivity parameter $\partial CLR/\partial T_g \approx \alpha_{T_g}$ (Figure 4a) is highest in the middle and high latitudes (ranging from 1.2 to 1.6 Wm^{-2} per 1°C change in T_g) and lowest over the tropical land masses. This is consistent with our previous analysis of the various contributions to the CLR (Figure 2) and reflects the latitudinal dependence of the atmospheric moisture content. The explained variance is shown in Figure 4b. Remarkably, the regression line (5) explains more than 90% of the variance over most areas (Figure 4b). These results suggest that the sensitivity of CLR to changes in T_g can be reasonably estimated by the simple linear approximation (5) of the radiative transfer equation.

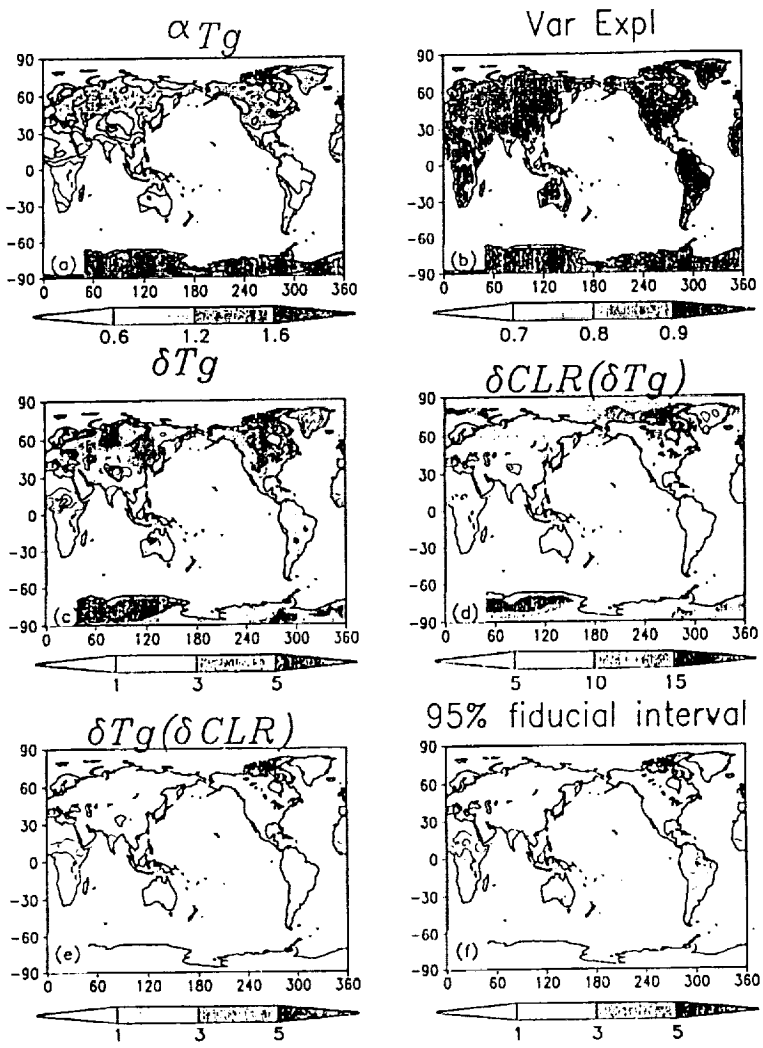

Figure 4. Estimation of δT_g based on linear fit: (a) αT_g ($Wm^{-2}\,°C^{-1}$), contour intervals are 2 $Wm^{-2}\,°C^{-1}$; (b) total variance explained; (c) monthly mean δT_g (°C); (d) estimated $\delta CLR(\delta T_g)$ (Wm^{-2}) based on Figures 4a and 4c; and (e) errors (°C) in estimation of δT_g based on Figure 4d and (f) 95% fiducial interval. Contours are for negative values in Figures 4c–4f; the intervals are the same as the shaded values.

We are interested in the ability of the regression to represent the systematic difference in the CLR fields. Figure 4c shows the mean ground temperature difference δT_g between the two data sets for January 1998. The mean temperature differences are quite large over the cold continents accounting for most of the differences in CLR over those regions. Figure 4d shows the mean CLR difference from the regression equation evaluated for the time mean δT_g. Comparison with Figure 1b shows that the linear approximation (the regression line) with just δT_g provides a good approximation to the time mean differences in CLR over land. The reader is reminded that the results in Figure 1b are computed with the radiative transfer equation and include the effects of q, T, and T_g. We shall see in the next section that the differences in T_g for the most part reflect a cold bias in this version of GEOS2.

We next obtain an estimate of δT_g by inverting the regression equation (5): i.e., by solving for δT_g using the estimate of α_{T_g}. For brevity we refer to this estimate of δT_g as the "retrieved" value. Figure 4e shows the difference between our retrieved δT_g and the actual values shown in Figure 4c. The magnitude of the errors in δT_g are in most regions less than 1°C. Figure 4f shows that the 95% fiducial intervals for the inverse regression [*Draper and Smith*, 1981] or retrieved values are typically ±3°C. Note that here we only show one side of the two-sided confidence interval corresponding to the sign of the actual error in Figure 4c.

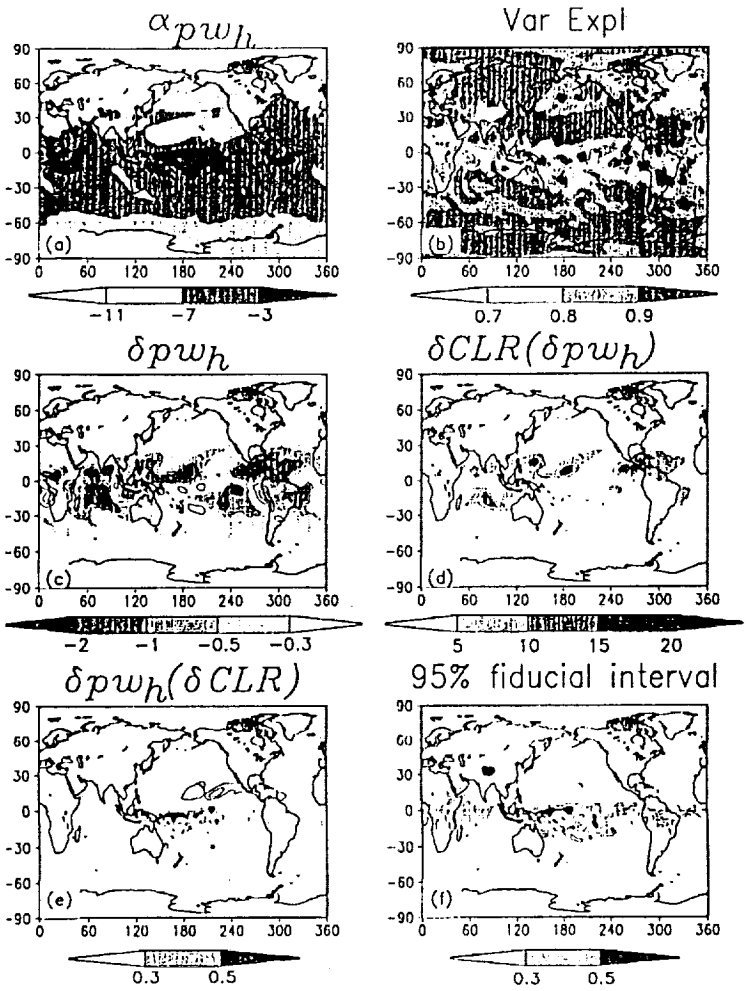

Figure 5. Same as in Figure 4 except for δpw_h: units are (Wm^{-2} mm^{-1}). Contour intervals are for values opposite to the shaded values.

F5 Figure 5 is the same as Figure 4 except for the mean moisture difference in the layer between 200 and 500 hPa (δpw_h). Figure 5a shows the sensitivity parameter (α_{pw_h}) determined from the regression

$$\delta \mathrm{CLR}(\delta pw_h) = \alpha_{pw_h} \delta pw_h + \varepsilon. \quad (6)$$

The spatial pattern of the sensitivity to upper level moisture is largely zonally symmetric, with the lowest sensitivity (<3 Wm^{-2}/mm precipitable water in the 200–500 hPa layer) in the convective regions of the tropics, and increasing sensitivity away from the tropics. A region of enhanced sensitivity (>9 Wm^{-2}/mm precipitable water in the 200–500 hPa layer) occurs over the subtropical regions of the North Pacific. We note that bands 2, 7, and 8 (Figure 2) show a tendency for enhanced contributions to the CLR from the subtropics especially over the North Pacific, suggesting the increased sensitivity is coming largely from these bands. Figure 5b shows that the regression line explains more than 90% of the variance in the CLR over most of the globe. Scattered regions of the tropics and subtropics, the extratropical storm tracks, and the Himalayas, explained variance less than 80%. With those exceptions the linear approximation to the full radiative transfer calculations for the impact of the upper level moisture appears to be quite good. Figure 5c shows the mean difference in the upper level moisture (δpw_h). The differences tend to be negative (GEOS2 is wetter) and largest just outside the tropics. The results of the regression for the time mean $\delta \mathrm{CLR}(\delta pw_h)$ (Figure 5d) again show a good approximation to the full calculation (Figure 1c), suggesting that much of the systematic difference between GEOS2 and ECMWF CLR over the subtropics are a result of differences in the upper level moisture. The results of the inverse calculation (Figure 5e) show that the magnitude of the errors in the retrieval of δpw_h is in most regions less than 0.5 mm. Figure 5f displays the 95% fiducial intervals on the retrieved values. The typical values range from 0.3 to 0.5 mm.

Figure 6 is the same as Figure 5 except for the mean mois- F6

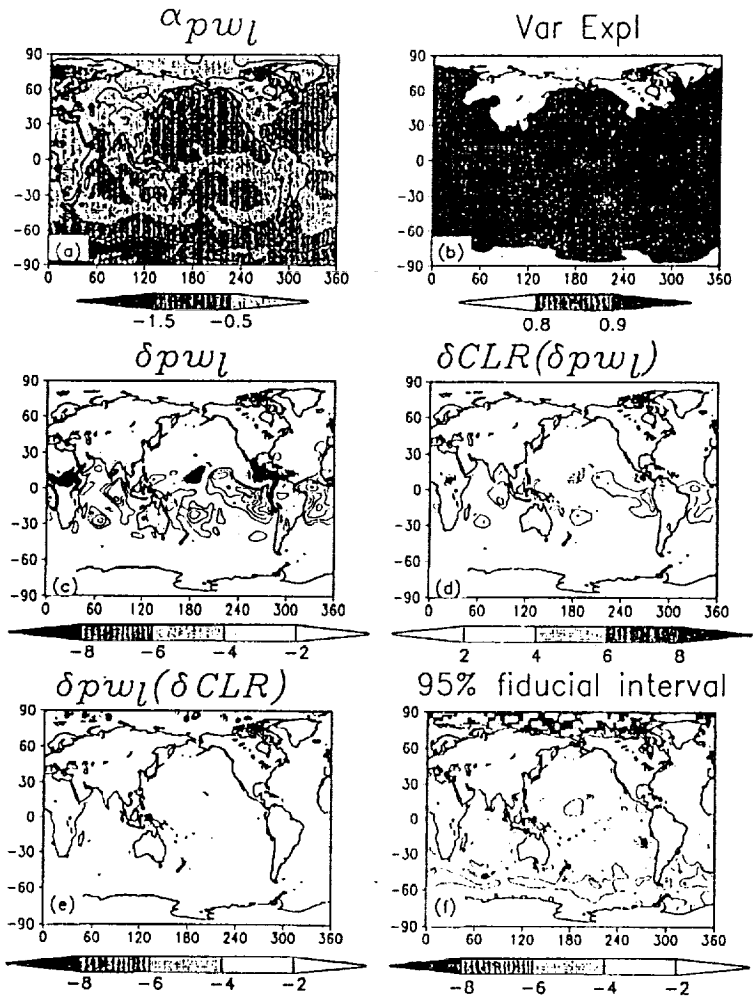

Figure 6. Same as in Figure 4 except for δpw_l: units are (Wm^{-2} mm^{-1}). Contour intervals are for values opposite to the shaded values.

ture difference in the layer between 500 hPa and the surface (δpw_l). Figure 6a shows that the sensitivity parameter (α_{pw_l}) is about an order of magnitude smaller than the upper level sensitivity parameter (α_{pw_h}). The greatest sensitivity (magnitude >1 to 2 Wm^{-2}/mm precipitable water) occurs at high latitudes in regions that are probably ice covered. Figure 6b shows the variance explains by the regression line which explains more than 90% of the variance in the CLR over most of the subtropics. Generally, less than 80% of the variance is explained over the cold continents and the polar regions. Figure 6c shows the mean difference in the lower-level moisture (δpw_l). The differences tend to be positive (GEOS2 is drier) throughout much of the tropics and subtropics, with the largest values occurring off the west coasts of Africa and South America in regions characterized by the presence of low-level stratus clouds. There are some regions with negative values in the Northern Hemisphere subtropics that coincide with large negative values at upper levels (compare Figure 5c). The results of the regression for the time mean δCLR(δpw_l) is shown in Figure 6d. This shows that some of the negative values along the west coasts of Africa, South America, and Africa in the full calculation (Figures 1a and 1c) are due to the differences in the low-level moisture. Figure 6e shows that the magnitude of the errors in the retrieval of δpw_l is in most regions less than 2 mm. The 95% fiducial intervals (Figure 6f) are in the range ±2–4 mm with the largest uncertainties in the Southern Hemisphere and the north polar region.

We next look more closely at the vertical dependence of the sensitivity of CLR to moisture. The panels on the left-hand side of Figure 7 show the differences between the ECMWF and the GEOS2 time mean moisture. The sensitivity parameters are the slopes of the regression lines through the scatterplots of δCLR versus δpw (panels on the right-hand side of Figure 7). These are computed, in this case, from the monthly mean fields, and each point in the scatterplots represents a different grid point (ocean only). This clearly shows that δCLR F7

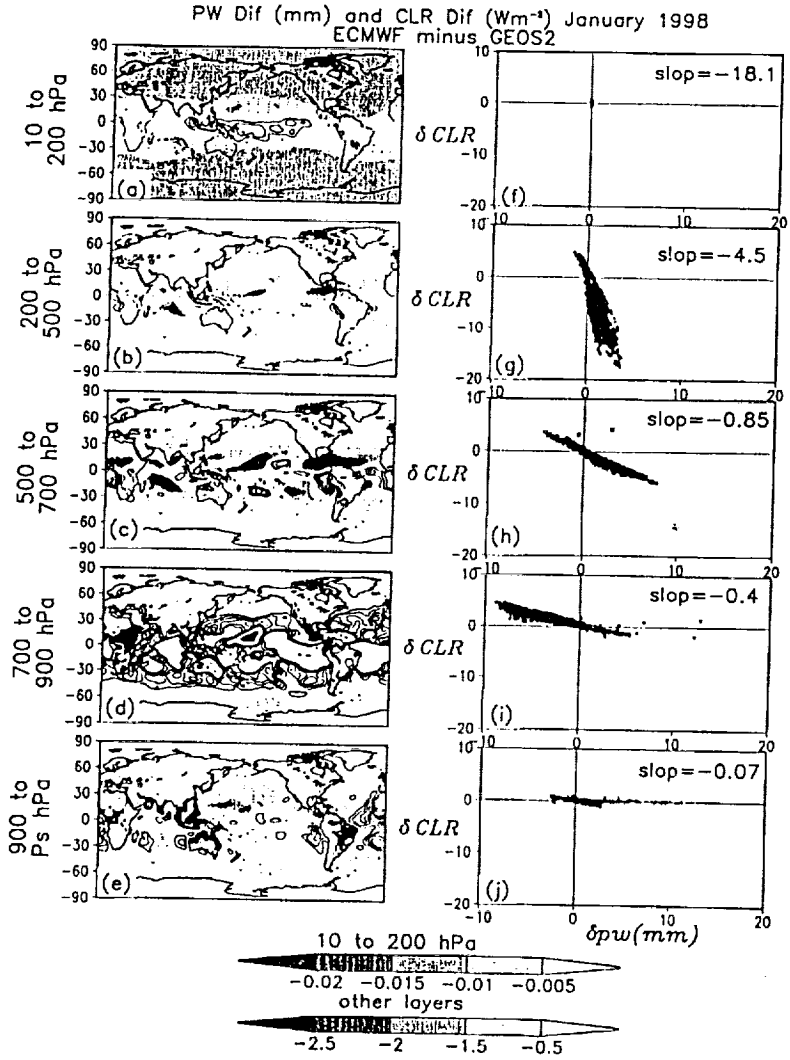

Figure 7. Sensitivity of δCLR (Wm^{-2}) to δpw (mm). The left-hand side are precipitable water (pw) differences between ECMWF and GEOS2; the right-hand side are scatterplots of δCLR and δpw. Contour intervals are for values opposite to the shaded values.

is most sensitive to δpw in the top layers. The sensitivity decreases the farther the layer is from the top of the atmosphere. Thus the moisture in the layer close to the surface tends to have little effect on CLR, consistent with our previous analysis of the contributions to the total CLR (Figure 2). Also, above 200 hPa the amount of moisture is too small to have an appreciable impact on the CLR despite the strong sensitivity. This is illustrated in Figure 8, which shows the relative contributions by layer to the time mean difference in the CLR due to moisture differences. Between 50 and 90% of the major CLR differences are due to pw differences between 200 and 500 hPa and another 10–30% comes from the layer between 500 and 700 hPa.

We next extend the results of the previous analysis to consider the case where, in addition to the total CLR measurements, we also have available CLR measurements for the window region. Figure 9 shows the sensitivity parameters computed separately for the window region (RadWn, left-hand side panels) and for the total CLR minus RadWn (right-hand side panels). The latter consists of the rotation and vibration and rotation (RVR) bands or nonwindow bands; see discussion of Figure 2). A comparison of Figures 9a and 9d shows that the T_g sensitivity in the window region tends to peak in middle latitudes, while in the nonwindow or RVR, the sensitivity shows a general increase with latitude. As such, the greatest sensitivity to T_g over the United States, Europe, and parts of China occurs in the window region. A comparison of Figures 9b and 9e with Figure 5a shows that the pw_g sensitivity is dominated by the RVR bands or nonwindow bands. Over the tropical oceans the sensitivity to the low-level moisture is greatest in the window region (compare Figures 9c and 9f). The large sensitivity over the eastern North Pacific and Atlan-

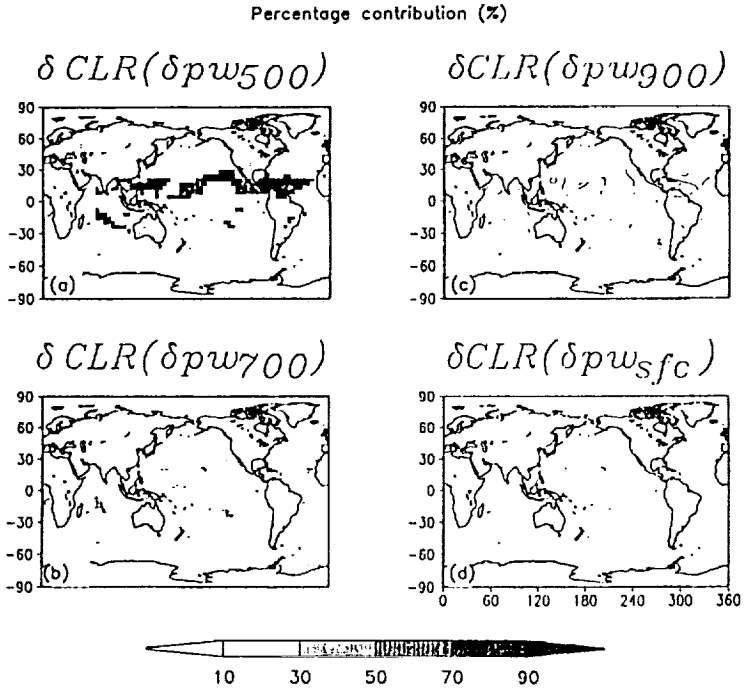

Figure 8. Relative contribution (%) of layer δpw to δCLR. Contour intervals are for values opposite to the shaded values.

tic seen in the total CLR calculation (Figure 6a) is due to the nonwindow bands or RVR bands (Figure 9f).

By considering the linearization (2) for both the RadWn and the RVR bands, we obtain two equations relating the CLR differences in each band to changes in the geophysical parameters. If we further limit the approximation of the CLR change to be primarily the result of just two geophysical parameters, we can estimate or "retrieve" these parameters. The previous results suggest that over land the CLR differences can be approximated by

$$\delta \mathrm{RadWn} = \alpha_{T_g(\mathrm{RadWn})}\delta T_g + \alpha_{pw_h(\mathrm{RadWn})}\delta pw_h, \quad (7)$$

$$\delta \mathrm{RVR} = \alpha_{T_g(\mathrm{RVR})}\delta T_g + \alpha_{pw_h(\mathrm{RVR})}\delta pw_h, \quad (8)$$

while over ocean, the approximation is

$$\delta \mathrm{RadWn} = \alpha_{pw_l(\mathrm{RadWn})}\delta pw_l + \alpha_{pw_h(\mathrm{RadWn})}\delta pw_h, \quad (9)$$

$$\delta \mathrm{RVR} = \alpha_{pw_l(\mathrm{RVR})}\delta pw_l + \alpha_{pw_h(\mathrm{RVR})}\delta pw_h. \quad (10)$$

Note that in the above relationships the sensitivity parameters (the α_x in Figure 9) are obtained from the 6 hourly data according to (5). By inverting (7)–(8) and (9)–(10), we obtain the retrieved estimates of the differences in the geophysical parameters assuming the α_x and δRadWn and δRVR are known. For example, the retrieved monthly mean differences in the geophysical parameters (T_g, pw_h, and pw_l) are shown in Figure 10 (left panels). The actual differences in T_g, pw_h, and pw_l from the full radiative transfer equation shown earlier are presented again in the right-hand panels to facilitate the comparison with the estimated values. The global mean bias in the retrieved δT_g is −0.04°C. The global mean root-mean-square error is 1.77°C, which corresponds to about 7% of the standard deviation of the true values. The global mean bias in the retrieval of δpw_h is −0.1 mm. The rms error is 0.26 mm, which corresponds to about 8% of the standard deviation of the true values. Similarly, the global mean bias in the retrieval of δpw_l is 0.4 mm. The rms error is 2.15 mm, which corresponds to about 20% of the standard deviation of the true values. FIO

The above results show that (7) through (10) give a close approximation to the mean differences in the ground temper-

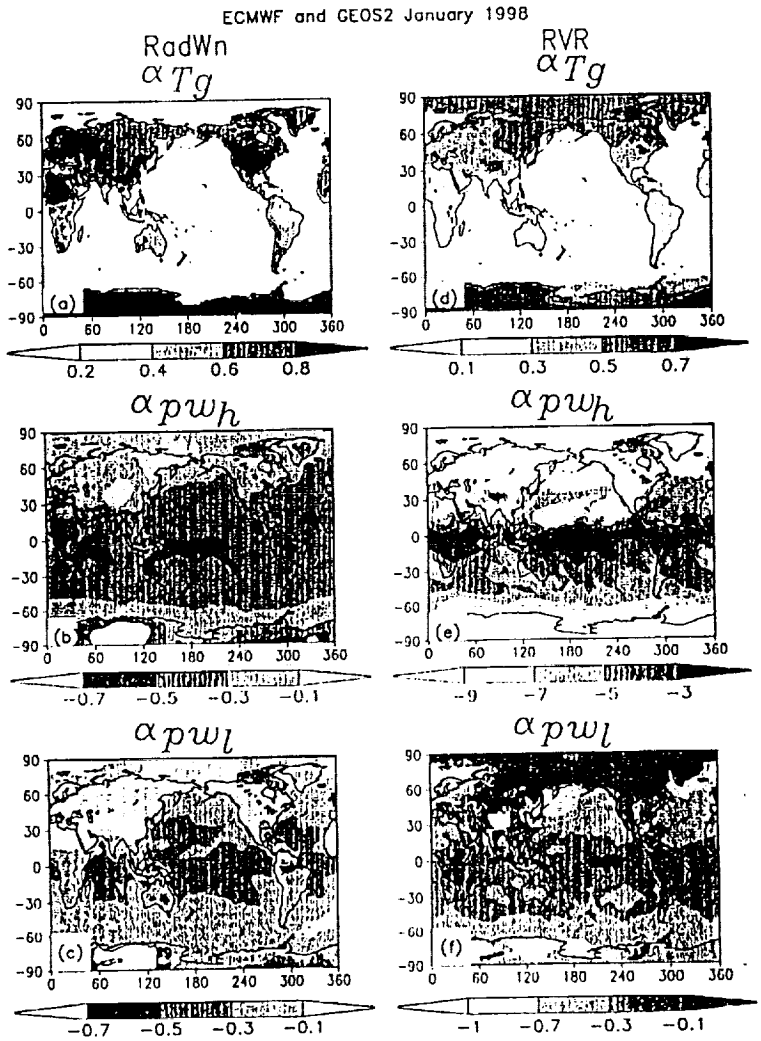

Figure 9. Coefficients of linear fit from Figures 9a to 9c are based on δRadWn and from Figures 9d to 9f are based on the rotation and vibration-rotational bands (δRVR): (a) αT_g (Wm^{-2} °C^{-1}), (b) αpw_h (Wm^{-2} mm^{-1}), (c) αpw_l (Wm^{-2} mm^{-1}), (d) αT_g (Wm^{-2} °C^{-1}), (e) αpw_h (Wm^{-2} mm^{-1}), and (f) αpw_l (Wm^{-2} mm^{-1}).

ature and moisture and suggest that these relationships can be used to infer errors in the geophysical parameters. In the following section we examine the differences between the synthetic GEOS2 CLR and the CLR from a preliminary CERES/TRMM data set.

5. A Comparison With CERES/TRMM CLR and RadWn

In the previous section we compared synthetic clear-sky fluxes (CLR and RadWn) computed from two 4-DDA data sets to develop some simple but quantitative measures of the sensitivity of clear-sky fluxes to changes in ground temperature and moisture. Insight into the sensitivity of the clear-sky fluxes to changes in these geophysical quantities was obtained by computing separately the various band contributions to the clear-sky fluxes. Reasonable approximations to the sensitivity of clear-sky fluxes to changes in the geophysical parameters were obtained with simple linear relationships using ground temperature and moisture in two broad layers of the atmosphere (the upper and lower troposphere) to predict the clear-sky flux changes in the RadWn and RVR bands (or non-window bands): the single predictor relationships (5) and (6) as well as the two parameter relationships (7) through (10).

We found that compared with ECMWF, GEOS2 has substantially colder ground temperature during January 1998, with differences ranging from 3°C to more than 7°C over high latitudes. Over these regions the sensitivity of CLR to T_g is between 1.2 and 1.8 Wm^{-2} per 1°C, so differences in the CLR range from about 5 to 15 Wm^{-2} in these regions, while parts of

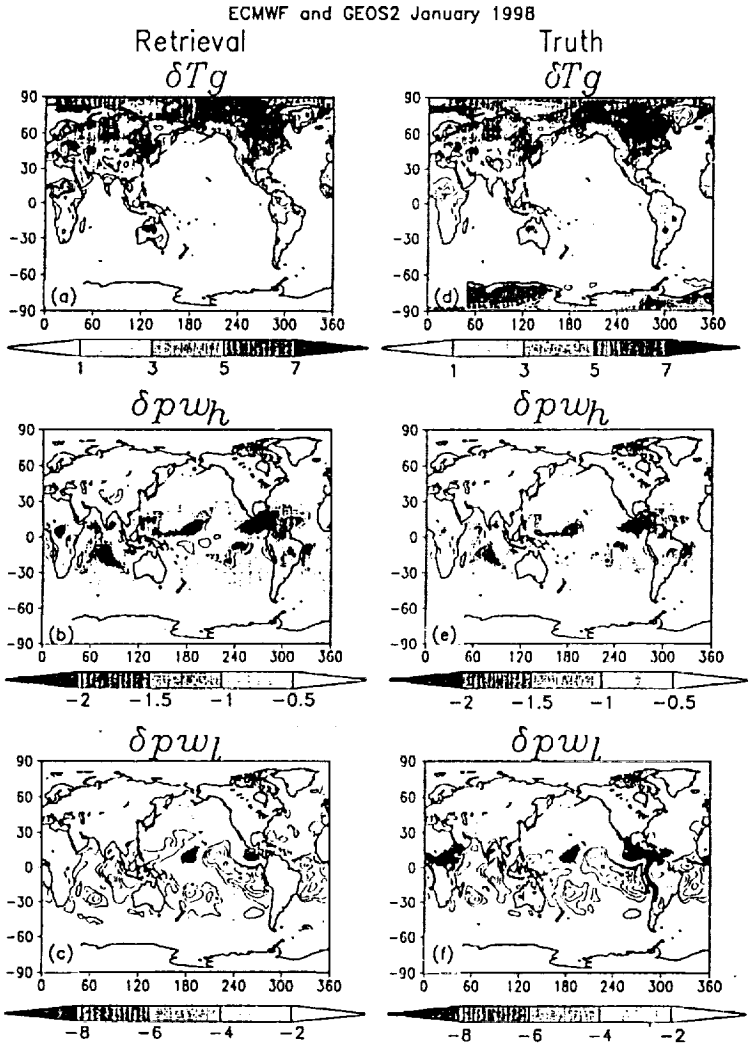

Figure 10. Retrieval of (a) δT_g (°C); contour intervals are 1°C; (b) δpw_h (mm); contour intervals are 1 mm; and (c) δpw_l(mm); contour intervals are 2 mm. True values of (d) δT_g (°C); (e) δpw_h (mm); and (f) δpw_l (mm).

the Antarctic show differences exceeding 20 Wm^{-2}. We also showed (Figures 10e and 10f) that compared with ECMWF, GEOS2 is wetter in the upper troposphere during January 1998 with differences as large as 2.5 mm over the tropical oceans. In the lower troposphere, GEOS2 is drier over most of the tropical oceans, with differences as large as 10 mm.

The above results give us confidence in the methodology, though they only provide us with difference (or "error") fields relative to the ECMWF products. We will now use some preliminary CERES/TRMM total CLR and RadWn data for January 1998 (in place of the ECMWF analysis data) to evaluate the quality of the GEOS2 ground temperature over land and moisture over the oceans.

F11 The results for the moisture are shown in Figure 11. We will validate our results against the SSM/I total precipitable water (TPW). For purposes of illustration and to demonstrate the reliability of our algorithm, we first apply our methodology to the synthetic δCLR and δRadWn data. Here we assume that the ECMWF data are the ground truth. The results Figure 11c) show that indeed, we have adjusted the GEOS2 TPW field to be close to that of ECMWF.

We next demonstrate our algorithm by applying it to the satellite data (CLR and RadWn) and assume that the satellite data are the ground truth. Figures 11d–11f show the results of applying our algorithm using the January 1998 CERES observations of δCLR and δRadWn. Figure 11d indicates that our moisture between 200 and 500 hPa is excessive over the tropical regions. Figure 11e indicates that at low levels GEOS2 is too dry in subtropical regions around ±20°–30° in both hemispheres. The corrected GEOS2 TPW (based on Figures 11d and 11e) is shown in Figure 11f. Comparing with Figure 11a, we see that the corrections have removed the major bias in the GEOS2 TPW fields. We note some amount of overcorrection, especially in the Northern Hemisphere subtropics.

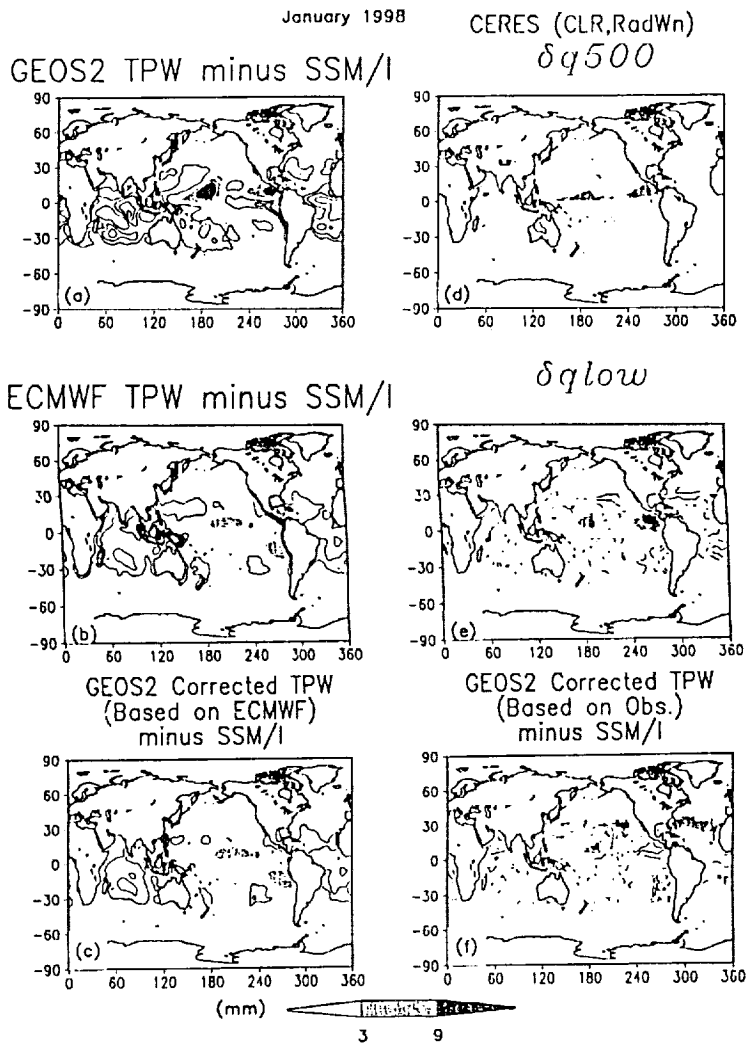

Figure 11. Diagnose of q: synthetic studies of TPW differences (mm): (a) GEOS2 minus SSM/I, (b) ECMWF minus SSM/I, and (c) GEOS2 corrected TPW based on ECMWF data minus SSM/I, and satellite-based TPW and layer (d) retrieved δpw_u based on δCLR and $\delta RadWn$ from CERES, (e) the same as Figure 11d except for δpw_l, and (f) GEOS2-corrected TPW based on Figures 11d and 11e. Contour intervals are for negative values, which are opposite to the shaded values.

Finally, we diagnose T_g for January 1998. Since we do not have global ground temperature observations, we will again compare with the ECMWF analyses. Figure 12a is the difference map of the retrieved δT_g minus actual (Figure 10a minus Figure 10d) based on the ECMWF data. As noted previously, the global mean bias is −0.04°C, and standard deviation is 1.25°C. This again gives us confidence that our algorithm can correct the ground temperature to within those error limits. Figure 12b is the mean difference in the CLR between GEOS2 and the CERES observations over the land areas between 40°S and 40°N (the fraction of the globe covered by the CERES instrument). Differences are negative over the Sudan, Saudi Arabia, and India. Positive values occur over southeastern Australia, southern Africa, the Andes, Central America, northern South America, and the Tibetan highlands. Figure 12c shows the implied GEOS2 T_g errors using the algorithm described above. The errors are quite large in some areas. For example, over the Sudan GEOS2 is more than 10°C too cold, while over southeast Australia, GEOS2 is more than 12°C too warm. Determining the errors in these estimates of the GEOS2 ground temperature bias will require, among other things, reliable estimates of the bias in the CERES measurements.

6. Discussion and Conclusions

We have introduced a simple but quantitative method for relating errors in model-based estimates of clear-sky longwave fluxes (CLR and RadWn) to errors in geophysical parameters. The primary motivation for this work is the underlying assumption that by linking the radiation errors to errors in the geo-

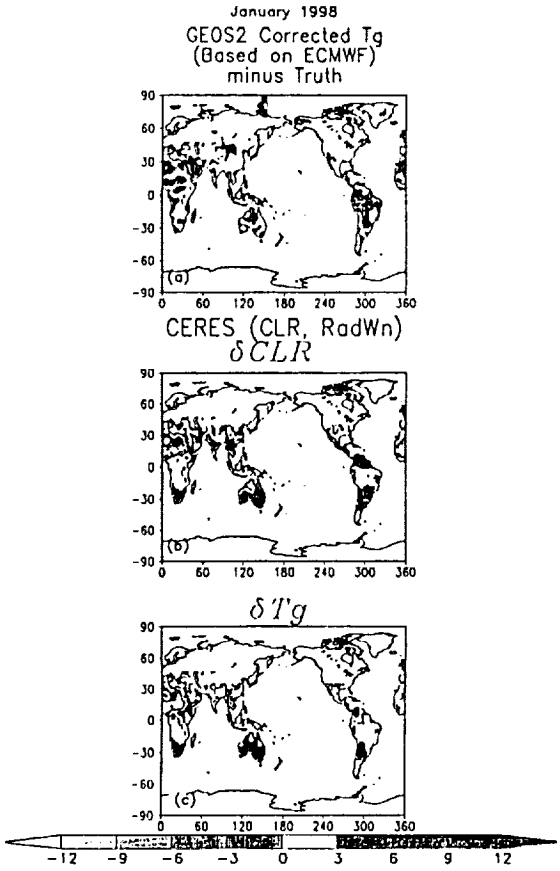

Figure 12. Diagnose of T_g: synthetic studies of δT_g (°C) based on ECMWF: (a) GEOS2-retrieved δT_g minus δT_g between ECMWF and GEOS2. Satellite diagnose of δT_g: (b) δCLR between CERES and GEOS2, and (c) retrieved δT_g. Contour intervals are for negative values, which are opposite to the shaded values.

physical parameters, we can provide greater insight to the model developer on potential model errors. We show for a test case (January 1998) that the method can potentially be used to obtain quantitative estimates of errors in ground temperature (δT_g) and moisture (δpw) from satellite observations. In particular, our analysis of synthetic total and window region clear-sky flux differences (computed from two different assimilated data sets) shows that a simple linear regression employing δT_g and broad layer δpw provides a good approximation to the full radiative transfer calculations, typically explaining more than 90% of the 6 hourly variance in the flux differences. These simple regression relations can be inverted to "retrieve" the errors in the geophysical parameters. Uncertainties (normalized by standard deviation) in the monthly mean retrieved parameters range from 7% for δT_g to about 20% for the lower tropospheric moisture (δpw_l).

Our initial application of the methodology employed an early CERES/TRMM data set (total and window region clear-sky longwave fluxes) to assess the quality of the GEOS2 data. The results showed that over the tropical and subtropical oceans, GEOS2 is, in general, too wet in the upper troposphere (mean bias of 0.99 mm) and too dry in the lower troposphere (mean bias of −4.7 mm). We note that these errors, as well as a cold bias in the ground temperature, have largely been corrected in the current version of GEOS2 with the introduction of a land surface model, a moist turbulence scheme and the assimilation of SSM/I total precipitable water.

The methodology described in this paper was developed as a result of our efforts to validate monthly mean fields from the GEOS2 global data assimilation system, but the methodology should also prove useful for validating the climatological fields of global atmospheric models. The accuracy of the methodology depends on the accuracy of the radiation code, surface emissivity, the ozone profile, as well as the accuracy of the satellite estimates of total and window region clear-sky longwave fluxes. While the initial results are promising, further work is required to fully assess the sensitivity to errors in the input parameters and to account for the mismatch between satellite observations and grid-scale model fields.

Acknowledgments. The authors thank the CERES Instrument Team (in particular, Bruce Wielicki, Tom Charlock, David Kratz, and Takmeng Wong) for providing early versions of the clear-sky OLR and window flux data.

References

Bruhl, C., et al., Halogen Occultation Experiment ozone channel validation, *J. Geophys. Res.*, *101*, 10,217–10,240, 1996.

Chou, M.-D., and L. Kouvaris, Calculations of transmission functions in the IR CO_2 and O_3 bands, *J. Geophys. Res.*, *96*, 9003–9012, 1991.

Chou, M. D., and M. Suarez, An efficient thermal infrared radiation parameterization for use in general circulation models, *NASA Tech. Memo. 104606*, vol. 3, 84 pp., 1994.

Chou, M.-D., W. Ridgway, and M.-H. Yan, Parameterizations for water vapor IR radiative transfer in the middle atmosphere, *J. Atmos. Sci.*, *52*, 1159–1167, 1995.

Cohn, E. Stephen, A. da Silva, J. Guo, M. Sienkiewicz, and D. Lamich, Assessing the effects of data selection with the DAO physical-space statistical analysis system, *Mon. Weather Rev.*, *126*(11), 29 3–2926, 1998.

Courtier, P., E. Andersson, W. Keckley, J. Pailleux, D. Vasiljevi, M. Hamrud, A. Hollingworth, F. Rabier, and M. Fasher, The I CMWF implementation of three-dimensional variational assimilat on (3d-Var), part I, Formulation, *Q. J. R. Meteorol. Soc.*, *124*, 1783–1807, 1998.

Data Assimilation Office (DAO), *Algorithm Theoretical Basis Document for Goddard Earth Observing System Data Assimilation System (GEOS DAS) With a Focus on Version 2*, 310 pp., NASA Goddard Space Flight Cent., 1996.

Draper, N. R., and H. Smith, *Applied Regression Analysis*, 709 pp., John Wiley, New York, 1981.

Ellingson, R., J. Ellis, and S. Fels, The Intercomparison of Radiation Codes in Climate Models (ICRCCM): Longwave results, *J. Geophys. Res.*, *96*, 8929–8953, 1991.

Gates, W. L., et al., An overview of the results of the Atmospheric Model Intercomparison Project (AMIP I), *Bull. Am. Meteorol. Soc.*, *80*, 29–55, 1999.

Helfand, H. M., A. Molod, and M. Bosilovich, Implications of a moist turbulence parameterization for the numerical prediction of the structure of the atmospheric boundary layer, paper presented at AMS 13th Conference on Numerical Weather Prediction, Am. Meteorol. Soc., Denver, Colo., September 13–17, 1999.

Koster, R. D., and M. J. Suarez, Modeling the land surface boundary in climate models as a composite of independent vegetation stands, *J. Geophys. Res.*, *97*, 2697–2715, 1992.

Kratz, D. P., M.-D. Chou, M. M.-H. Yan, and C.-H. Ho, Minor trace gas radiative forcing calculations using the *k*-distribution method with one-parameter scaling, *J. Geophys. Res.*, *103*, 31,647–31,656, 1998.

Lau, W. K.-M., Y. C. Sud, and J.-H. Kim, Intercomparison of hydro-

logic processes in global climate models, *NASA Tech. Mem. 104617*, 170 pp., 1995.
Riishøjgaard, L. P., I. Štajner, and G.-P. Lou, The GEOS Ozone Data Assimilation System, *Adv. Space Res.*, *25*, 1063–1072, 2000.
Salisbury, J. W., and D. M. D'Aria, Emissivity of terrestrial materials, in the 8–14 micron meter atmospheric window, *Remote Sens. Environ.*, *42*, 83–106, 1992.
Schubert, S. D., J. Pfaendtner, and R. Rood, An assimilated data set for Earth Science applications, *Bull. Am. Meteorol. Soc.*, *74*, 2331–2342, 1993.
Štajner, I., and L. P. Riishøjgaard, The GEOS ozone data assimilation system: Specification of error statistics, *Q. J. R. Meteorol. Soc.*, in press, 2000.
Takacs, L. L., and M. J. Suarez, Dynamical aspects of climate simulations using the GEOS General Circulation Model, *NASA Tech. Memo. 104606*, vol. 10, 70 pp., 1996.
Wentz, F., *User's Manual, SSM/I Geophysical Tapes*, 11 pp., Remote Sens. Syst., 1994.
Wielicki, B. A., B. R. Barkstrom, E. F. Harrison, R. B. Lee III, G. L. Smith, and J. E. Cooper, Clouds and the Earth's Radiant Energy System (CERES): An Earth Observing System Experiment, *Bull. Am. Meteorol. Soc.*, *77*, 853–868, 1996.
Wilber, A. C., D. P. Kratz, and S. K. Gupta, Surface emissivity maps for use in satellite retrievals of longwave radiation, *NASA Tech. Pap., NASA/TP-1999-209362*, 35 pp., 1999.
Zhou, J., Y. C. Sud, and K.-M. Lau, Impact of orographically induced gravity wave drag in the GLA GCM, *Q. J. R. Meteorol. Soc.*, *122*, 903–927, 1996.

C. I. Lin and I. Štajner, General Sciences Corporation, NASA Goddard Space Flight Center, Greenbelt, MD 20771.
S. Schubert and M. L. C. Wu, Data Assimilation Office, Code 910.3, Goddard Laboratory for Atmospheres, NASA GSFC, Greenbelt, MD 20771. (mwu@dao.gsfc.nasa.gov)

(Received December 8, 1999; revised August 2, 2000; accepted August 4, 2000.)